PNAS RESEARCH ARTICLE | EARTH, ATMOSPHERIC, AND PLANETARY SCIENCES

Magma-induced tectonics at the East Pacific Rise 9°50′N: Evidence from high-resolution characterization of seafloor and subseafloor

Milena Marjanović[a,b,1,2], Jie Chen[a,1], Javier Escartín[c], Ross Parnell-Turner[b], and Jyun-Nai Wu[b]

Edited by Michael Manga, University of California, Berkeley; München, Germany; received January 22, 2024; accepted April 25, 2024

At fast-spreading centers, faults develop within the axial summit trough (AST; 0 to 250 m around the axis) primarily by diking-induced deformation originating from the axial magma lens (AML). The formation of the prominent abyssal-hill-bounding faults beyond the axial high (>2,000 m) is typically associated with the unbending of the lithosphere as it cools and spreads away from the AST. The presence of faults is rarely mapped between these two thermally distinct zones, where the lithosphere is still too hot for the faults to be linked with the process of thermal cooling and outside of the AST where the accretional diking process dominates the ridge axis. Here, we reveal a remarkable vertical alignment between the distinct morphological features of the magma body and the orientation of these faults, by comparison of 3-D seismic imagery and bathymetry data collected at the East Pacific Rise (EPR) 9°50′N. The spatial coincidence and asymmetric nucleation mode of the mapped faults represent the most direct evidence for magmatically induced faulting near the ridge axis, providing pathways for hydrothermalism and magma emplacement, helping to build the crust outside of the AST. The high-resolution seafloor and subsurface images also enable revised tectonic strain estimates, which shows that the near-axis tectonic component of seafloor spreading at the EPR is an order of magnitude smaller than previously thought with close to negligible contribution of lava buried faults to spreading.

mid-ocean ridges | faulting | seismic imaging | magmatic system | high-resolution bathymetry

Faulting patterns and mechanics at mid-ocean ridges (MOR) are strongly influenced by spreading rate, which is in turn modulated by the melt availability within the magmatic system underneath (1–4). At melt-laden, fast-spreading centers (full spreading rate of >80 mm/y), such as the East Pacific Rise (EPR) 9°50′N (Fig. 1), the seafloor morphology starts to be dominated by an axial high, and the shallow-most magma bodies (or axial magma lens; AML) are typically located at ~1 to 1.5 km below seafloor (bsf; 5–8). Faulting is characterized by ridge-parallel, closely spaced (100s-m to a few km spacing; Fig. 1*A*) fault scarps with a vertical throw of ~10 to 100 m, defining linear abyssal hills. Although the tectonic contribution to overall spreading of these faults is estimated to be <5% (9–14), this brittle deformation plays a major role in shaping the seafloor (15–18). Hence these faults represent important potential pathways for interactions between the magmatic system and off-axis hydrothermal circulation (19, 20).

From numerous field observations and modeling, it was suggested that changes in the stress field due to overpressurization of the shallow-most magma body and associated diking represent the main controlling factor for cracking the layer above (27–29). While the doming of the central part of the magma body can explain the formation of fissures and faults vertically above, a different mechanism is in play to address the faulting outside of the AST (28). For instance, diking at the lateral margins of magma bodies as zones of stress instabilities can induce rotation of tensile stresses (σ_1) and result in fault planes with lower dipping angles (30).

Based on seafloor observations at the fast-spreading EPR, three distinct faulting mechanism are present within 20 km of the ridge axis (Fig. 1 *C* and *D*). The faults formed within the axial summit trough (AST) zone, at ~0 to 250 m from the ridge axis (marked as *Fa* in Fig. 1*C*), are attributed to vertical dike intrusions (11, 25, 31–33) rooting in the AML (26). Then, ~2 to 4 km away from the ridge axis (roughly the width of the axial high), the seafloor is dominated by inward and outward facing abyssal-hill faults (9, 34), attributed to the flexural bending of the brittle lithosphere (1, 35), which are marked as *Ff* (Fig. 1*D*); the *Ff′* marks the first pair of *Ff* (Fig. 1*C*). Between the faults developed within the AST zone *Fa* (31, 36) and the first abyssal-hill bounding fault *Ff′* (32), there is scarce surface evidence of predominant inward facing faulting that accommodates the tectonic component of plate

Significance

We provide the most direct evidence for magmatically controlled nucleation of faults near a fast-spread ridge, in the zone that is too hot for plastic deformation of the lithosphere to take place but far enough from the innermost axial zone to be explained by diking. This result is based on the remarkable spatial match between the seafloor fault scarps and three-dimensional morphology of the magma bodies. Thus, formed faults play a role in the formation of the crust away from the on-axis volcanic centers through magma channeling but much less so through tectonic deformations. Collectively, these findings contribute to our knowledge on how plate spreading is accommodated which is fundamental for understanding the global tectonic cycles.

Author affiliations: [a]Department of Marine Geosciences, Institut de Physique du Globe de Paris, Université Paris Cité, CNRS UMR 7154, Paris 75005, France; [b]Institute of Geophysics and Planetary Physics, Scripps Institution of Oceanography, University of California, San Diego, La Jolla, CA 92037; and [c]Laboratoire de Géologie, École Normale Supérieure/CNRS UMR 8538, L'université Paris Sciences & Lettres, Paris 75005, France

Author contributions: M.M. and J.E. designed research; M.M. and J.C. performed research; M.M. and J.C. analyzed data; M.M. collected seismic data; R.P.-T., J.-N.W. and M.M. collected bathymetry data; and M.M., J.C., J.E., R.P.-T., and J.-N.W. wrote the paper.

The authors declare no competing interest.

This article is a PNAS Direct Submission.

[1] M.M. and J.C. contributed equally to this work.

[2] To whom correspondence may be addressed. Email: marjanovic@ipgp.fr.

This article contains supporting information online at https://www.pnas.org/lookup/suppl/doi:10.1073/pnas.2401440121/-/DCSupplemental.

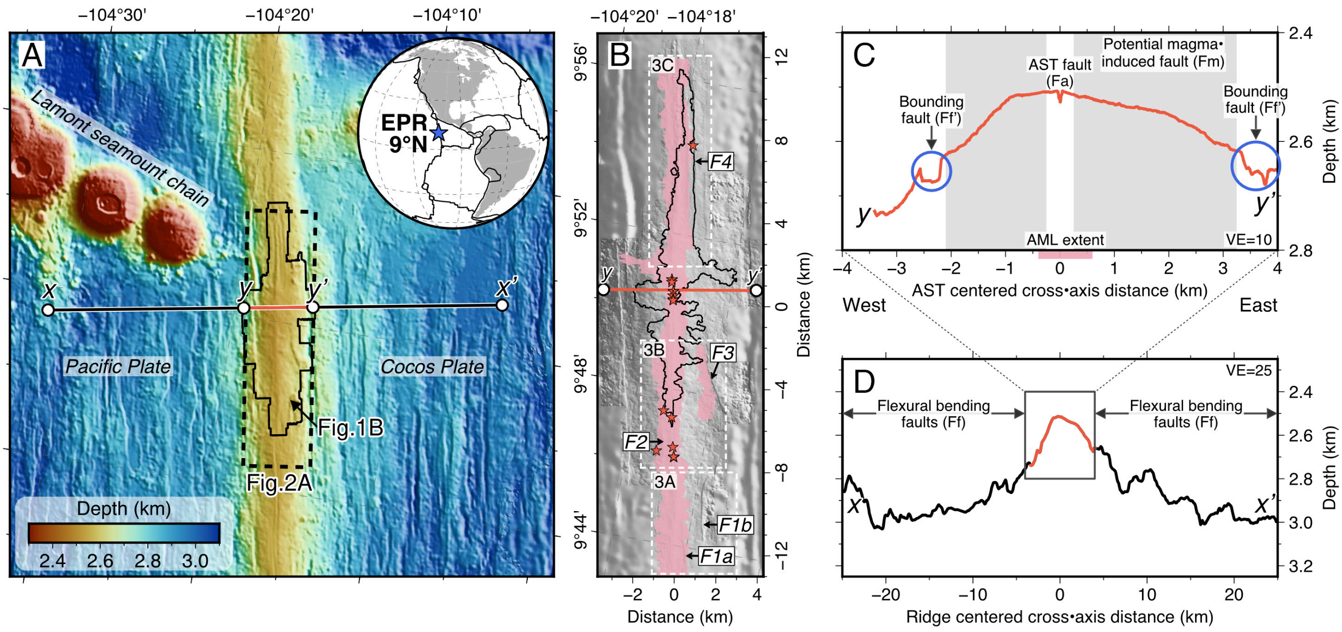

Fig. 1. Study area and modes of faulting. (*A*) Regional bathymetry map of the East Pacific Rise (EPR) 9°50′N (21), separating the Cocos and Pacific Plates. *Inset*: plate boundaries (black lines) (22); EPR 9°50′N is a blue star. Main panel: The dashed box is seismic volume where axial magma lens (AML) is imaged (Fig. 2*A*); the solid black line is AUV survey area (23), shown in panel (*B*). Part of the line marked in red as yy′ is shown in panel (*B*) and the bathymetry profile in (*C*); the solid line xx′ indicates the location of the cross-axis bathymetry profile displayed in panel (*D*). (*B*) Composite map obtained by combining the shipboard and AUV-derived bathymetric data (50 and 1 m resolution, respectively). Pink shadings show AML and the upper crustal off-axis magma lens (uOAML) imaged within the dike section shown in Fig. 2*A*; red stars mark known vent fields (24). Markers *F1a*, *F1b*, *F2*, *F3*, and *F4* indicate faults described in the text; the black line is extent of 2005-06 eruption (23, 25). The white dashed boxes show the location of Fig. 3. (*C*) Portion of the seafloor profile yy′ depicting the presence of the first pair of abyssal-hill-bounding faults (*Ff′*) and faulting within AST (*Fa*). The gray shaded zones indicate the regions where magma-induced faulting (*Fm*) is expected. The pink bar marks the width of the AML extracted from the seismic volume (26) along the same profile. (*D*) Seafloor depth profile extracted along the line xx′ (panel *A*). The black box indicates the location of the portion yy′ shown in panel (*C*). The extent of the region where flexural bending faults dominate is marked as *Ff*.

accretion (11); within this region, the young lithosphere remains hot and thin, inhibiting tectonic deformation (1, 9, 13) and it is also located outside of the AST to be affected by accretion diking. Seafloor mapping of such faults within this region shows that they contribute to plate separation with tectonic strain >2% (11). The studies speculated that the contribution may be significantly higher as many of the similar faults within this region may be covered by lava flows and invisible in the seafloor bathymetry data (9–12). The strain contribution of these buried faults and how some of the prominent faults develop within the warm axial zone remain unknown, primarily due to the lack of detailed images of these structures in the seafloor and subsurface.

Here, we study the fast-spreading EPR 9°50’N, where one of the most extensive and interdisciplinary efforts of the seafloor investigation has been put to map the seafloor morpho-tectonics and its crustal structure spanning two documented eruption events that occurred in 1991 to 1992 and 2005 to 2006 (6, 11, 25, 37–41). In anticipation of the next eruption event (19), this area has been extensively mapped at high resolution (~1 m) with AUVs (12, 23). These bathymetric data will provide a benchmark to evaluate volumes of future eruptions in the area (Fig. 1*B*). In addition, recent images of magma lenses beneath the eruption area (Figs. 1*B* and 2*A*) were presented from the seismic volume collected in 2008 (26). The results suggest that the morphology of this magma lens is controlled by melt delivery and melt withdrawal within a volcanic cycle. This complex AML geometry also controls dike nucleation and eruption within the volcanically modified AST developed at the ridge. However, the role of the AML architecture in faulting beyond the narrow accretion zone of the AST up to the first pair of the abyssal-hill-bounding faults has not been examined.

In this study, we combine analysis of 1-m-resolution multibeam bathymetric data (sourced from refs. (12) and (24), and two additional areas collected during the AT50-21 cruise; see *SI Appendix*) with 3-D imaging of magma bodies using a depth-migrated seismic volume (26). In addition to the recently published images of the magma bodies beneath the eruption area, here, we introduce 3-D image of the AML south of the eruption zone, covering the area from ~9°42’N to 9°56’N (Fig. 2 and *SI Appendix*, Fig. S1). We also show a detailed analysis of the faulting pattern based on the AUV high-resolution bathymetry data, linking them to the magmatic system and the subseafloor fault system. The methodologies behind seismic and bathymetry data processing, magma body horizons, and seafloor faults picking are provided in recent respective publications (12, 26). The information on data analyses specific to the presented work are provided in *SI Appendix*. The results of this joint study provide evidence for magmatically governed nucleation of the near-axis faults with implications for hydrothermalism and the build-up of the upper oceanic crust through volcanism outside of the narrow accretion zone.

Results and Discussion

Observations of the Tectono-Magmatic Linkages. We describe four morphological features of the magma bodies, mapped within the EPR 9°50’N axial region, which show remarkable spatial correspondence with the fault scarps mapped in the seafloor, and therefore point toward the existence of the tectono-magmatic genetic link.

The first zone we focus on is to illustrate the magmato-tectonic link extending from ~9°42 to 9°45’N (Figs. 2, 3*A*, and 4). Faults can be identified both in AUV-acquired bathymetric data (11), and we mark them as *F1a* and *F1b*, respectively (Fig. 3*A*). The northern limit of the AML segment is marked by the small-scale ridge-axis disruption at 9°44’N (6), where the AML splits into two limbs (Fig. 2 *B* and *E* and *SI Appendix*, Fig. S1). The shallowest western limb sits at ~1,400 m below the seafloor, whereas the

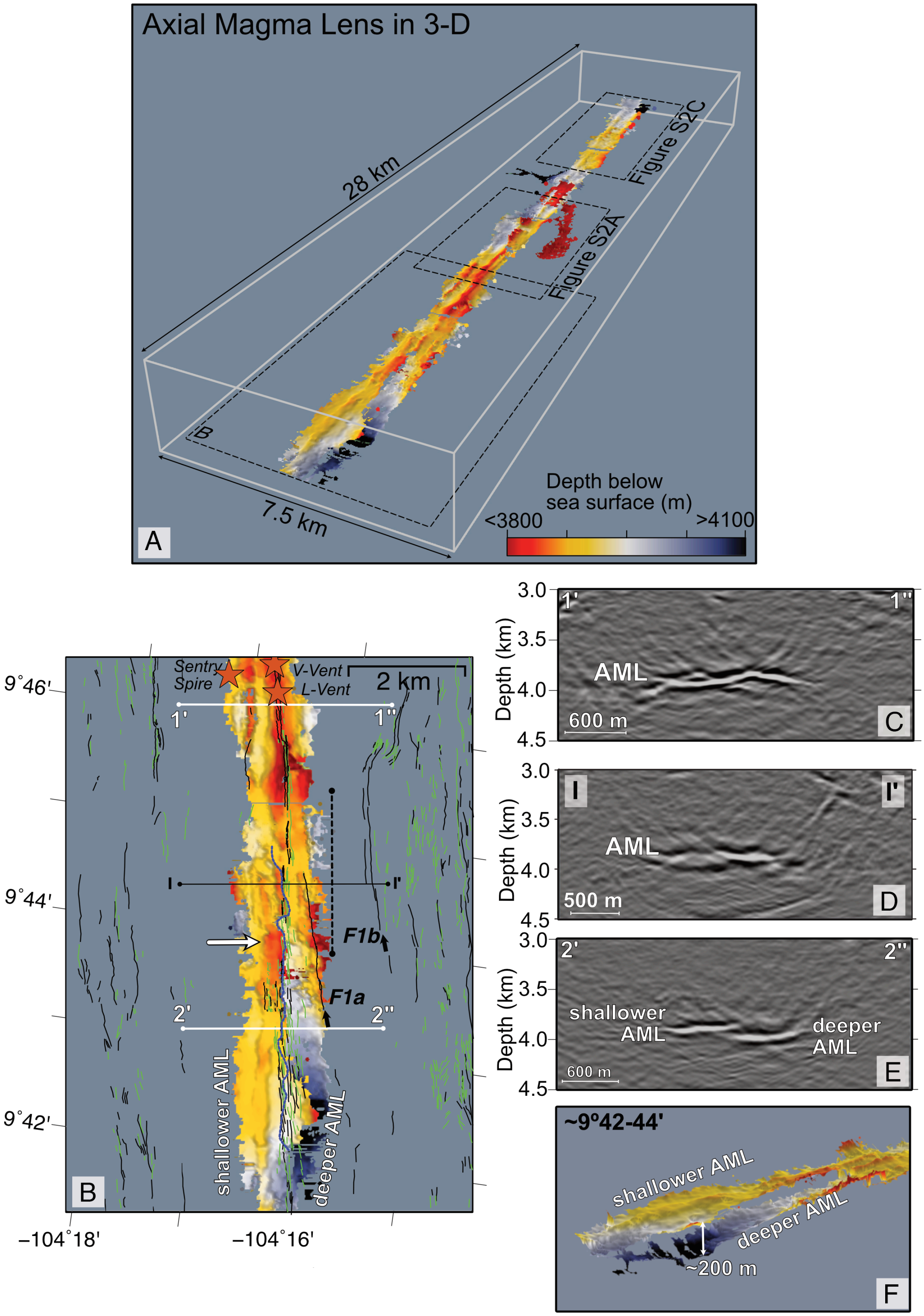

Fig. 2. Seismically imaged magma body beneath the EPR from ~9°42′ to 9°56.5′N. (*A*) Perspective view of the AML horizon extracted from the 2008 seismic volume. The dashed boxes mark the regions presented in more detail in panel (*B*), and in *SI Appendix*, Fig. S2 *A* and *C*. (*B*) Plan view of the magma body south of 9°46′N. The same panel is shown in *SI Appendix*, Fig. S1 without interpretation and transparent western AML limb. Red stars indicate vent fields (24); green and black lines represent fissures and faults, respectively (11, 12). The extent of the faults *F1a* and *F1b* are marked in black arrows; the dashed black line indicates the latitudinal extent of the fault plane imaged in the volume and shown in Fig. 4. The white arrow indicates the southern extent of the small-scale tectonic discontinuity observed in the seafloor (6). The white horizontal line 1′1″ indicates the location of the seismic profile extracted from the volume shown in panel (*C*). The horizontal black line marks the location of the seismic profile I-I′ shown in panel (*D*) and Fig. 4*A*. The white line 2′2″ and indicates the location of the seismic section shown in panel (*E*). The northern one (i.e., 1′1″) crosses the AML region dominated by ridge-like structures, whereas the southern one (i.e., 2′2″) shows the presence of two separate lenses. (*F*) 3-D view depicts the complexity in the magma body south of 9°44′N.

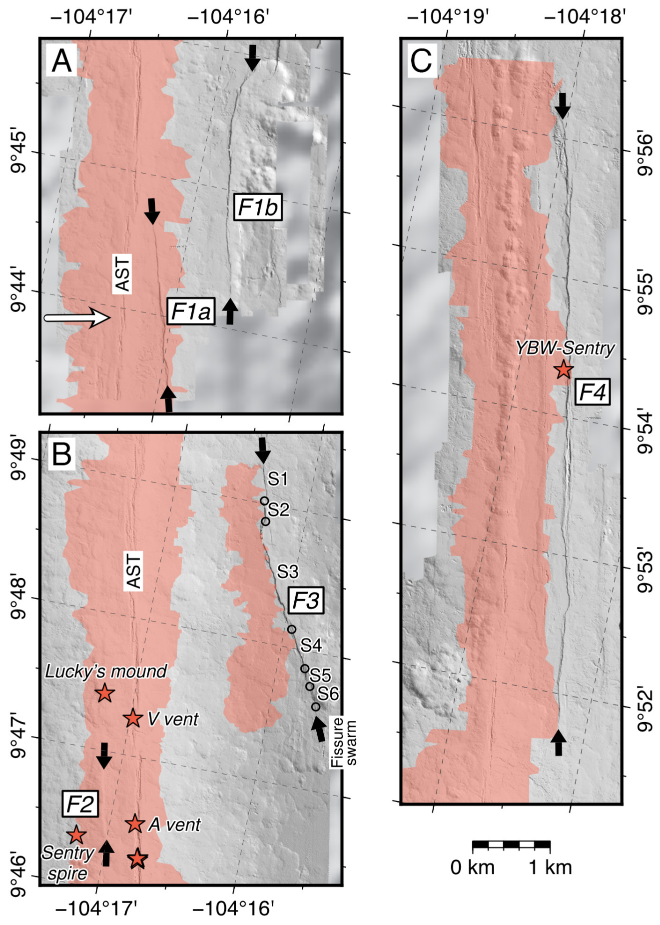

Fig. 3. Close-up views of magma-induced faults: (*A*) F1a and F1b, (*B*) F2 and F3, (*C*) F4. White arrow in (*A*), marks the small-scale tectonic discontinuity observed in the seafloor (6). The open circles in (*B*) along the Fault F3 mark the discontinuities in fault throw and geometry, subdividing the fault into six segments (S1–S6). The red stars mark the location of the confirmed, active vent fields (24). All maps are in the same distance scale. Pink areas outline seismically imaged the magma bodies.

deepest eastern limb from the bifurcation point plunges southward to <200 m below the average depth of the western limb (Fig. 2 *D* and *E* and *SI Appendix*, Fig. S1). For the western limb, the shallowest portion of the magma body is observed westward of the AST, whereas for the eastern limb, the shallowing is predominantly present along its eastern edge (Fig. 2*B*). The orientation of this eastern AML edge matches that of two parallel, inward-facing faults which trend obliquely (5 to 10°) to the AST, mapped in the seafloor bathymetry at ~800 and 1,700 m from the ridge axis (Figs. 2*B* and 3*A*). In pre-stack depth migrated seismic volume, we observe a reflector dipping ridge-ward that can be traced to the top of the AML over 3 km in the along-axis direction (Figs. 2*B* and 4 and *SI Appendix*, Fig. S3). When this reflector is projected upward, its intersection at the seafloor is collocated with the easternmost fault seafloor scarp *F1b* (Figs. 3*A* and 4*A*).

Based on this spatial match, and on the planar nature of the reflector, we infer the presence of a fault plane dipping at ~58°, extending to the depth of the AML at ~1.4 km below sea floor (Fig. 4*A*). The reflection signal could result from velocity contrast of the fault damaged zone and/or alteration front from hydrothermal mineralization as indicators of the venting are observed in its vicinity in the seafloor (12, 24). Given the spatial relationship with the AML, we cannot rule out the possibility that this fault plane has been used as a channel for magma migration outside of the narrow accretion zone and mapped in the seismic image. Lava flows east of the fault scarp are visible in the available near-bottom bathymetry data and support the above (Fig. 3*A*). We are unable to image the uppermost part of the fault due to the overprinting triplication signal originating from a high vertical velocity gradient zone characterizing the upper crust (42). The above does not preclude the near vertical *F1a* plane connecting the AML edge with the fault scarp closer to the ridge axis.

The second example of AML-fault coincidence is at the segment extending from 9°46.3 to 9°48.5'N (Fig. 3*B* and *SI Appendix*, Fig. S2*A*). On the seafloor, by re-examining the high-resolution bathymetry data, we identify the presence of the fault scarp *F2* limited in extent, with a vertical offset of <5 m (Fig. 3*B*). Directly beneath *F2,* there is a ridge-like structure, we identify in the AML (*SI Appendix*, Fig. S2). This feature is located 500 m west of the AML center and represented by two limbs (*SI Appendix*, Fig. S1), running roughly parallel to the axis-centered diking root zone (26). Projecting a plane that connects the AML feature beneath

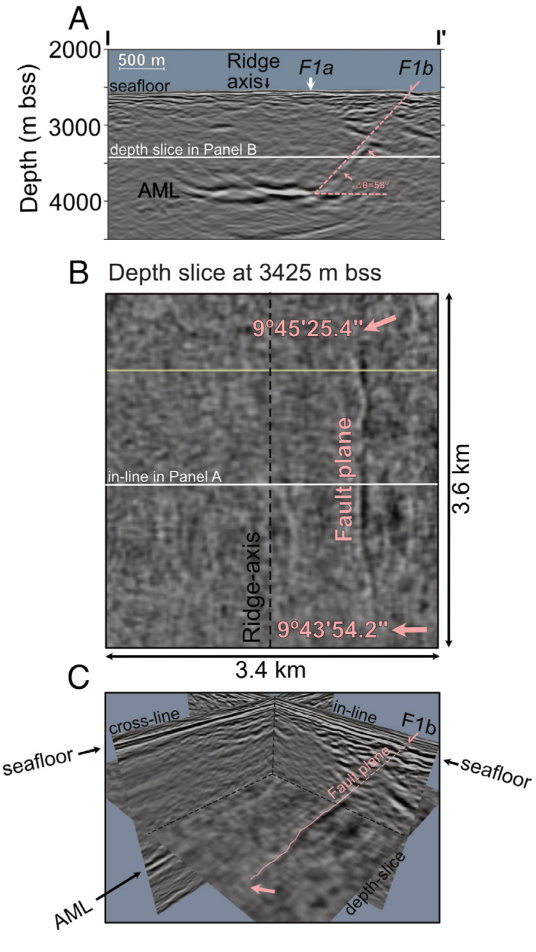

Fig. 4. Imaging fault plane in the seismic volume. (*A*) Seismic section extracted from the volume in cross-axis direction (i.e., inline; location marked in Fig. 2*B*) showing the presence of the AML and ridge ward dipping reflection signal in the upper crust, we interpret as a fault plane, F1b. In white arrow, we mark the surface location of the F1a. (*B*) The depth slice extracted from the volume at 3,425 m below the sea surface showing continuous linear feature, we interpret as fault plane, delimited by pink arrows. The intersections between the inline (panel *A*) and depth slice (panel *B*) are indicated in white horizontal lines in both panels. The ridge axis is marked in black dashed line. The yellow line does not have interpretation significance—it marks the merging front of two parts of the volume uploaded separately due to graphic memory limitations. (*C*) Intersections between inline, depth slice, and crossline (ridge parallel direction) to emphasize the linearity of the reflector (marked in pink line) and provide evidence against the possibility for the event to represent diffraction tail artifact. The same panels without interpretation are shown in *SI Appendix*, Fig. S3.

the western flank and the scarp of *F2*, we obtain an apparent dip of ~74° (*SI Appendix*, Fig. S4*A*). On the surface, the fault is surrounded by several active hydrothermal vent sites, including Sentry Spire and Lucky's Mound (Fig. 3*B* and *SI Appendix*, Fig. S2*A*). Moreover, the fault plane appears to be dotted by bathymetric constructs that are classified as likely and possible active vent fields (24). This abundance of vents along the scarp could indicate that the fault plane has been used as a hydrothermal pathway and is spatially associated with the source of heat at depth, i.e., AML, similar to YBW-Sentry field (19).

The most remarkable match between the fault trace and the geometry of the magma body is observed at ~9°48'N (Fig. 3*B* and *SI Appendix*, Fig. S2*A*). The obliquely trending fault scarp (*F3* in Fig. 3*B*) closely follows the eastern edge of the steeply, southward dipping off-axis magma lens (uOAML) emplaced within the dikes at 600 to 1,100 m bsf (26). This vertical alignment suggests that the fault plane dip is ~90°. Based on the imaged reflectors connecting the AML and uOAML (*SI Appendix*, Fig. S2*B*), one portion of the magma was probably sourced from the AML (26). The two OAMLs imaged in the lower crust (43) directly below this shallow magma body (26) could have provided additional input of melt.

In addition, along the northernmost part of the fault (latitudinal extent 9°48'28.8-58"), we conduct temperature measurements using three temperature loggers (*SI Appendix*). The results display a prominent thermal anomaly right above the shallowest portion of the uOAML (*SI Appendix*, Fig. S2*A*), with the peak at the locus of the highest fault throw (Fig. 5 and *SI Appendix*, Fig. S5).

In the northernmost part of the study area, we observe an *en echelon,* ridge-parallel fissure system and associated fault (*F4* in Fig. 3*C* and *SI Appendix*, Fig. S2*C*) at ~500 and 750 m from the ridge axis, respectively (*SI Appendix*, Fig. S2*C*). They closely follow the eastern edge of the AML, which represents the shallowest part of the lens in this region (26). The spatial correlation suggests that this was the eruptive fissure system that funneled melt to the surface during the 2005–06 eruption (25). The newly discovered high-temperature vent site (YBW-Sentry) is in the vicinity of the fault, which may have channeled down- and up-flow pathways, controlling the hydrothermal circuit (19, 26). While the fault plane is not imaged seismically, its projection from the fault scarp to the easternmost tip of the AML would yield a ~72° dip (*SI Appendix*, Fig. S4*B*). The high-angle dip can explain the absence of the fault plane signature in the seismic data (*SI Appendix*).

Evidence for Fault Geometry Governed by the Architecture of Magma Body. The four cases of AML-fault interaction described above develop asymmetrically (three on the eastern and one on the western flank), the mode of near-axis deformation that cannot be attributed to the conventional plate accretion processes. Based on these observed spatial tectono-magmatic links, the nucleation of the deformation is likely to be associated with the three-dimensional relief of the magma body, with a geometry consistent with the orientation of surface fault scarps (Fig. 3 *B* and *C* and *SI Appendix*, Fig. S2). The imaged fault plane at 9°42–45'N, linking the surface scarps and the easternmost edge of the AML, suggests that the magma lenses play a role in the nucleation and evolution of near-axis faults. The pronounced ridge-like morphology in the AML penetrates the overlying dike section as observed in ophiolites (45), promoting tensile stresses at the shallower parts vertically above, facilitating faulting (9, 46), which in turn may further impact the shape of the AML.

To further explore the relationship between magma morphology and near-axis tectonic features expressed in the seafloor, we analyze the 9°48'N example (F3) as the magma body is located in the shallow dike section. Along the fault scarp, we map six segments (S1–S6) using 1-m resolution bathymetric data (Figs. 3*B* and 5). Segmentation of the fault scarp is consistently associated with a morphological change in the upper crustal magma lens: its width, depth, and/or geometry, corroborating the genetic relationship. In addition, the observed near-bottom temperature increase (up to 200th of a degree; collected in early 2024) is spatially collocated with the shallowest part of the uOAML (Fig. 5*C* and *SI Appendix*, Fig. S5). This observation indicates that magma body is still present (>15 y after the data were collected) and contains some amount of melt. The peripheral segments (S1 and S6) show the smallest throw (2 to 3 m on average), reaching a maximum in the segment center (<6 m) and gradually diminishing toward the fault tip (Fig. 5*C*). For the remaining segments (S2–S5) the throw at segments' centers is on average ~15 m, with

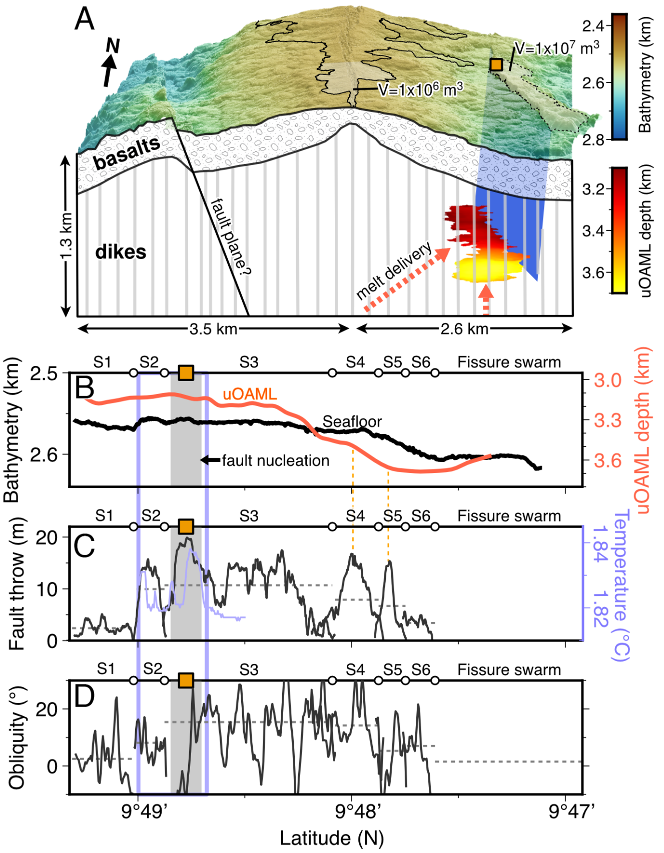

Fig. 5. Tectono-magmatic link of the oblique-trending *F3* at 9°48'N. (*A*) Three-dimensional ridge-perpendicular schematic diagram showing the main features of the seafloor and the subseafloor and lava flow outline, based on AUV high-resolution bathymetry and seismic volume. The orange square marks the location of the fault nucleation. The potential fault plane obtained as an extension of its surface expression in depth (not imaged in seismic) is shown on the west flank in dashed line. The lava volume emplaced on the seafloor through this fault system (white shaded area) is estimated as 1 × 10^7 m^3, using the "PILE VOLUME" of Global Mapper software. The lava volume near the AST (white shaded area) was estimated as 1 × 10^6 m^3 (23). Dashed red arrows indicate potential melt delivery pathways from the main AML (arrow on the left of the uOAML) and from previously reported lower crustal OAMLs (44). (*B*) Depths of the seafloor and uOAML along the *F3*. The gray shaded zone marks the fault nucleation zone. (*C* and *D*) Fault throw and obliquity along the *F3*, respectively. The pale purple line in panel (*C*) shows measured temperature along the northernmost part of the fault scarp recorded on the probe closest to the seafloor (*SI Appendix*). The two vertical bars in the same color delimit the latitudinal extent of the higher temperature anomaly. Vertical dashed orange lines mark correlation between higher fault throws and abrupt changes in the uOAML depth for segments S4 and S5. Gray dashed lines show the average values for each fault segment (S1–S6). The average obliquity of the fissure swarm is also included.

the maximum throw of nearly 20 m beneath the northernmost part of segment S3 (at 9°48.75'N; Fig. 5 *B* and *C*). This location is also where the magma body reaches the shallowest point at ~600 m bsf (Fig. 5*B* and *SI Appendix*, Fig. S2*A*), suggesting that this is the nucleation depth of the fault. Observations of terrestrial dike intrusions show that the initiation of faults is typically associated with the shallowest portion of the dike intrusion (e.g., the East African rift system and the Iceland volcanic system) (27, 47). Here, we also observe the highest peak in the near-bottom temperature (Fig. 5*C* and *SI Appendix*, Fig. S5), which further supports the presence of shallow intrusion. At this nucleation point, the fault throw is expected to be largest, as observed (Fig. 5*C*) and it is anticipated for the fault to grow laterally (48, 49). We propose that the horizontal intrusion of a sill into the dikes could perturb stresses at depth, which creates a zone of instability directly above. Land studies suggested that accumulated stresses are large enough to break intact rock, although modeling challenged this view and instead pointed toward reactivation of sealed fractures (here possibly inherited from the tectono-magmatic processes in the AST domain) as a more plausible scenario (29). North of the sill injection site or fault nucleation (S1 and S2), magma maintained its shallow depth and propagated in a direction following the dominant ridge stresses, resulting in upper crustal unzipping parallel to the ridge axis and gradually reducing the throw. South of the injection site (S3–S5), the magma body was emplaced at greater depths trending obliquely, with local enhanced throw that is collocated with the abrupt changes in uOAML depth (Fig. 5). The unzipping followed the oblique direction dictated by the easternmost edge of the magma body.

What controlled the oblique sill emplacement is not clear. One explanation could be the stresses introduced by the magma channeling from the AML (*SI Appendix*, Fig. S2*B*). The influx of magma from the lower crustal reservoirs could contribute further (26, 44). Regardless of the origin, this prominent obliquity helps eliminate the "structural valve" scenario, under which the oblique trending is tectonically governed. It is difficult to envision the state of stresses under which a fault plane could have developed in a direction other than parallel to the ridge and only on one of the flanks. Finally, it is important to note that unzipping of the crust did not follow all the way to the southern tip of the magma body but ceased several hundred meters prior to the termination, departing from the magma body edge and terminating in a ridge-parallel fissure swarm (12). The melt has been delivered to the surface from the uOAML along the fault plane. Assuming a uniform subsidence of the seafloor with age, we estimate that the minimum of 10×10^6 m^3 of lava volume was emplaced on the seafloor through this fault system (Fig. 5*A*), which makes 6 to 20% of the total volume of the adjacent AML segment (52 to 157 $\times 10^6$ m^3) (26) and 21 to 63% of the estimated uOAML volume range (*SI Appendix*). This volume could have been expelled through several eruption phases in the past.

Based on the available shipboard bathymetry data, the traces of the magmatically induced faults are not preserved beyond the first appearance of the first pair of the abyssal-hill-bounding fault, which suggests that they are location-specific features, which become sealed away from the reach of the stress field induced by the magma intrusions (Fig. 1*A*). The two generations of the obliquely trending faults within 9°44'N region (Figs. 2*B* and 3*A*) provide an example of the magmatically induced fault scarps preserved within the first 4 km away from the ridge axis. The presence of two fault generations may also indicate that the faults are formed during the periods of magma recharge and disappear during the waning phase, arguing for persistent morphological features of the replenished AML. The fault with the lower dip angle was probably developed as an additional, more recent feature at just about the right distance from the easternmost edge of the AML for dipping angle of ~60°.

The changes in magma body morphology, associated with magma replenishment, and their effect on much longer-lived tectonics can be tackled only after high-resolution images of magma bodies in pre- and posteruptive settings become available. Finally, based on our observations, the presence of asymmetric faults, peaking from the background bathymetry within the 250 to 4,000 m zone could be used as good indicators of the morphological structures of the AML elsewhere and help us understand the near to off-axis venting sites, such is the case with the newly discovered YBC-Sentry vent (19).

Implications for Tectono-Magmatic Accretion. The tectonic strain in crustal accretion along the EPR 9°50'N was estimated at ~2 to 4%, assuming a uniform dip of 45° (11, 13). However, the ubiquitous absence of most fault planes in seismic data (*SI Appendix*) and the near-bottom imagery (12) consistently suggest fault dips >70° in the subseafloor and on the seafloor. We, therefore, recalculate the tectonic strain of a 3-km long ridge section near the EPR 9°50'N with AUV 1-m resolution bathymetric data that cover 3 to 4 km of seafloor from the ridge axis (dashed outline in Fig. 6). We pick the bottom and top of the fault scarps and the outline of the fissures as polygons (Fig. 6*B*), based on a previous study (12). We measured fault throw (D) and fissure width (W) along across-axis profiles spaced at $C = 2$ m. Within the mapped area (A), we calculate the apparent tectonic strain (T) based on apparent faults and fissures expressed as

$$T = 100\,\% \times \frac{(C\ \Sigma D/\tan(\alpha) + C\ \Sigma W)}{A},$$

where α is the fault dip, here equal to 70°, and $\sum D$ and $\sum W$ represent sums of fault throw and fissure width, respectively, within the mapped area A outlined by a dashed box in Fig. 6 *A*–*C*.

The resulting apparent tectonic strain is 0.4%. Using the typically assumed dip of 45°, the tectonic strain would be close to 1%, which is comparable to the estimate presented in a recent study (12). Finally, we used depth-migrated seismic reflection data to image lava-buried faults (Fig. 6*C*). In the seismic data, we pick only the features with evident steps in seafloor reflectors we attribute to faulting (Fig. 6 *D*–*G*). Independent fault identification using near-bottom bathymetric and seismic reflection data have an excellent agreement (Fig. 6*C*), except that the seismic reflection shows more outward dipping faults (Fig. 6 *D*–*G*), likely buried by lavas. Assuming a fault throw of 7.2 m (average of the seafloor exposed faults) and a fault dip of 70°, we estimate the total tectonic component of extension to be 0.46%. This finding shows that the contribution of buried faults is 0.06% and hence nearly negligible. Although there are probably additional small-scale lava-buried faults near the AST zone undetected by our seismic imagery, their contribution to tectonic components is expected to be even smaller than 0.06%, both due to the throw size and their primarily magmatic origin.

Data, Materials, and Software Availability. The seismic and bathymetry data and the interpreted AML horizon picks are available at Marine Geoscience Data System at: https://doi.org/10.1594/IEDA/314654 (50), https://doi.org/10.26022/IEDA/330373 (51), https://doi.org/10.26022/IEDA/331330 (52), and https://doi.org/10.60521/331596 (53).

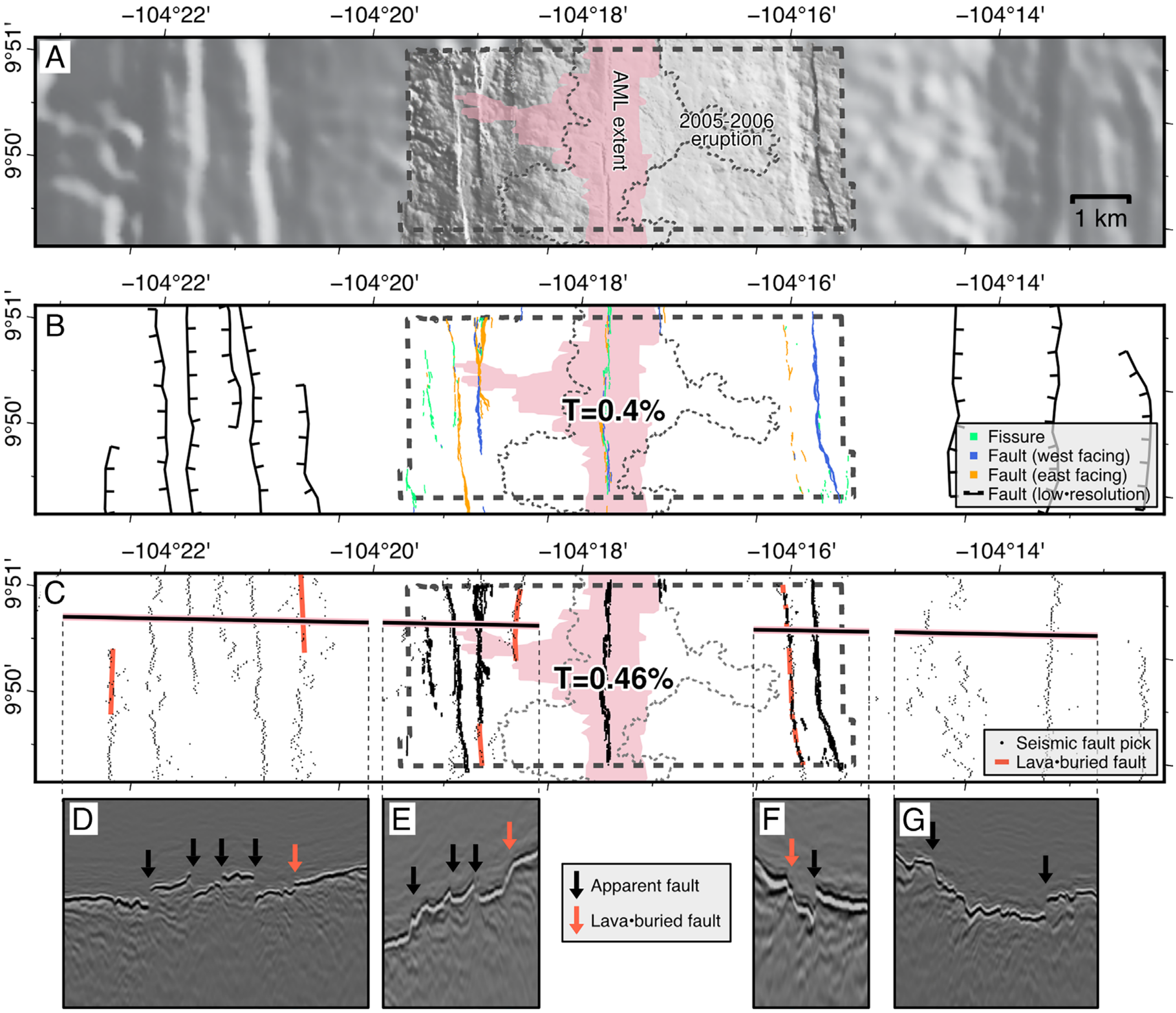

Fig. 6. Faulting pattern and tectonic strain in crustal accretion at the EPR 9°50′N. (*A*) Shaded bathymetry map. AUV high-resolution data are superimposed on low-resolution ship-borne data. The pink area indicates the AML extent; dashed gray line marks the contour of the lava flow (23). (*B*) Faulting pattern (faults and fissures), interpreted from bathymetry data. See legend for symbols. (*C*) Seismic fault picks. Red lines indicate lava-buried faults that are invisible in bathymetry data. (*D*–*G*) Cross-sections showing examples of seismic fault picks under the same distance scale. Black arrows indicate faults visible in both bathymetry and seismic data. Red arrows indicate lava-buried faults only visible in seismic data.

ACKNOWLEDGMENTS. The study was partially supported by Marie S. Curie Individual Fellowship awarded to M.M. (proposal no: 655283 3DWISE; 2015-2017). The funding for the data acquisition used in this study was provided by the following NSF grants: OCE-1948936 to R.P.-T. We would like to thank Suzanne Carbotte, Daniel Fornari, and Yann Klinger for insightful discussions and two anonymous reviewers for constructive comments that improved the manuscript. We would also like to thank the chief scientist of the cruise AT50-21 cruise Jill McDermott, Daniel Fornari and Thibaut Barreyre, for providing additional near-bottom bathymetry datasets. Finally, we would like to extend our gratitude to the Sentry team and the entire crew of the AT50-21 research cruise aboard R/V Atlantis. The interpretation and analyses of seismic data were made in OpendTect. For producing figures, we used the Generic Mapping Tools (GMT), OpendTect, and Affinity Design. This is IPGP contribution #4285.

1. W. R. Buck, L. L. Lavier, A. N. B. Poliakov, Modes of faulting at mid-ocean ridges. *Nature* **434**, 719–723 (2005).
2. Z. Liu, W. R. Buck, Global trends of axial relief and faulting at plate spreading centers imply discrete magmatic events. *J. Geophys. Res. Solid Earth* **125**, e2020JB019465 (2020).
3. C. Small, "Global systematics of mid-ocean ridge morphology" in *Faulting and Magmatism at Mid-Ocean Ridges, Geophysical Monograph Series*, W. R. Buck, P.T. Delaney, J.A. Karson, Y. Lagabrielle, Eds. (AGU, Washington, D. C., 1998), pp. 1–25.
4. J. A. Goff, Regional variations in the spreading-rate dependence of abyssal hill roughness as indicators of mantle heterogeneity. *Geophys. Res. Lett.* **50**, e2023GL102801 (2023).
5. M. Marjanović *et al.*, Crustal magmatic system beneath the East Pacific Rise (8°20′ to 10°10′N): Implications for tectonomagmatic segmentation and crustal melt transport at fast-spreading ridges. *Geochem. Geophys. Geosyst.* **19**, 4584–4611 (2018).
6. S. M. Carbotte *et al.*, Fine-scale segmentation of the crustal magma reservoir beneath the East Pacific Rise. *Nat. Geosci.* **6**, 866–870 (2013).
7. J. C. Mutter *et al.*, Seismic images of active magma systems beneath the east pacific rise between 17°05′ and 17°35′S. *Science (80-)* **268**, 391–395 (1995).
8. R. S. Detrick *et al.*, Multi-channel seismic imaging of a crustal magma chamber along the East Pacific Rise. *Nature* **326**, 35–41 (1987).
9. D. W. R. Bohnenstiehl, S. M. Carbotte, Faulting patterns near 19°30′S on the East Pacific Rise: Fault formation and growth at a superfast spreading center. *Geochem. Geophys. Geosyst.* **2**, 1056 (2001).
10. M. Le Saout, R. Thibaud, P. Gente, Detailed analysis of near tectonic features along the East Pacific Rise at 16°N, near the mathematician hot spot. *J. Geophys. Res. Solid Earth* **123**, 4478–4499 (2018).
11. J. Escartín *et al.*, Interplay between faults and lava flows in construction of the upper oceanic crust: The East Pacific Rise crest 9°25′–9°58′N. *Geochem. Geophys. Geosyst.* **8**, Q06005 (2007).
12. J. N. Wu *et al.*, The role of on- and off-axis faults and fissures during eruption cycles and crustal accretion at 9°50′N, East Pacific Rise. *Geochem. Geophys. Geosyst.* **24**, e2022GC010794 (2023).
13. S. M. Carbotte, K. C. Macdonald, Comparison of seafloor tectonic fabric at intermediate, fast, and super fast spreading ridges: Influence of spreading rate, plate motions, and ridge segmentation on fault patterns. *J. Geophys. Res. Solid Earth* **99**, 13609–13631 (1994).
14. P. A. Cowie, A. Malinverno, W. B. F. Ryan, M. H. Edwards, Quantitative fault studies on the East Pacific Rise: A comparison of sonar imaging techniques. *J. Geophys. Res.* **99**, 15205 (1994).
15. J. A. Olive, P. Dublanchet, Controls on the magmatic fraction of extension at mid-ocean ridges. *Earth Planet. Sci. Lett.* **549**, 116541 (2020).
16. M. D. Behn, G. Ito, Magmatic and tectonic extension at mid-ocean ridges: 1. Controls on fault characteristics. *Geochem. Geophys. Geosyst.* **9**, 8–10 (2008).
17. G. Ito, M. D. Behn, Magmatic and tectonic extension at mid-ocean ridges: 2. Origin of axial morphology. *Geochem. Geophys. Geosyst.* **9**, 9–12 (2008).
18. E. S. Kappel, W. B. F. Ryan, Volcanic episodicity and a non-steady state rift valley along northeast pacific spreading centers: Evidence from sea MARC I. *J. Geophys. Res. Solid Earth* **91**, 13925–13940 (1986).

19. J. M. McDermott *et al.*, Discovery of active off-axis hydrothermal vents at 9° 54′N East Pacific Rise. *Proc. Natl. Acad. Sci. U.S.A.* **119**, e2205602119 (2022).
20. R. A. Sohn, K. W. W. Sims, Bending as a mechanism for triggering off-axis volcanism on the East Pacific Rise. *Geology* **33**, 93–96 (2005).
21. J. C. Mutter *et al.*, "Searching for changes in AMC characteristics on the EPR using comparisons of reflection images obtained in 1985 and 2008" in *AGU Fall Meet. Suppl., Abstract B21A-0321* (2008), p. A321.
22. P. Bird, An updated digital model of plate boundaries. *Geochem. Geophys. Geosyst.* **4**, 1027 (2003).
23. J. N. Wu *et al.*, Extent and volume of lava flows erupted at 9°50′N, East Pacific Rise in 2005–2006 from autonomous underwater vehicle surveys. *Geochem. Geophys. Geosyst.* **23**, e2021GC010213 (2022).
24. J.-N. Wu, R. Parnell-Turner, D. J. Fornari, T. Barreyre, J. McDermott, "Oceanic heat transfer by diffuse and focused flow through off-axis vents at 9°50'N East Pacific Rise" in *AGU Fall Meeting Abstracts* (2023), pp. V43B–0174.
25. S. A. Soule, D. J. Fornari, M. R. Perfit, K. H. Rubin, New insights into mid-ocean ridge volcanic processes from the 2005–2006 eruption of the East Pacific Rise, 9°46′N–9°56′N. *Geology* **35**, 1079–1082 (2007).
26. M. Marjanović *et al.*, Insights into dike nucleation and eruption dynamics from high-resolution seismic imaging of magmatic system at the East Pacific Rise. *Sci. Adv.* **9**, eadi2698 (2023).
27. A. M. Rubin, Dike-induced faulting and graben subsidence in volcanic rift zones. *J. Geophys. Res.* **97**, 1839–1858 (1992).
28. A. Gudmundsson, Formation and growth of normal faults at the divergent plate boundary in Iceland. *Terra Nov.* **4**, 464–471 (1992).
29. D. Trippanera, J. Ruch, V. Acocella, E. Rivalta, Experiments of dike-induced deformation: Insights on the long-term evolution of divergent plate boundaries. *J. Geophys. Res. Solid Earth* **120**, 6913–6942 (2015).
30. T. Parsons, G. A. Thompson, Does magmatism influence low-angle normal faulting? *Geology* **21**, 247–250 (1993).
31. D. J. Fornari, R. M. Haymon, M. R. Perfit, T. K. P. Gregg, M. H. Edwards, Axial summit trough of the East Pacific Rice 9°-10°N: Geological characteristics and evolution of the axial zone on fast spreading mid-ocean ridge. *J. Geophys. Res. Solid Earth* **103**, 9827–9855 (1998).
32. D. J. Fornari *et al.*, "Submarine lava flow emplacement at the East Pacific Rise 9° 50 ′N: Implications for uppermost ocean crust stratigraphy and hydrothermal fluid circulation" in *Geophysical Monograph Series,* C. R. German, J. Lin, and L. M. Parson, Eds. (AGU, Washington, D. C., 2004), pp. 187–217.
33. W. W. Chadwick, R. W. Embley, Graben formation associated with recent dike intrusions and volcanic eruptions on the mid-ocean ridge. *J. Geophys. Res. Solid Earth* **103**, 9807–9825 (1998).
34. K. C. Macdonald, P. J. Fox, R. T. Alexander, R. Pockalny, P. Gente, Volcanic growth faults and the origin of Pacific abyssal hills. *Nature* **380**, 125–129 (1996).
35. A. K. Shah, W. R. Buck, Plate bending stresses at axial highs, and implications for faulting behavior. *Earth Planet. Sci. Lett.* **211**, 343–356 (2003).
36. S. A. Soule, J. Escartín, D. J. Fornari, A record of eruption and intrusion at a fast spreading ridge axis: Axial summit trough of the East Pacific Rise at 9–10°N. *Geochemis. Geophys. Geosyst.* **10**, Q10T07 (2009).
37. O. Aghaei *et al.*, Crustal thickness and Moho character of the fast-spreading East Pacific Rise from 9°42′N to 9°57′N from poststack-migrated 3-D MCS data. *Geochem. Geophys. Geosyst.* **15**, 634–657 (2014).
38. M. Marjanović *et al.*, A multi-sill magma plumbing system beneath the axis of the East Pacific Rise. *Nat. Geosci.* **7**, 825–829 (2014).
39. V. L. Ferrini *et al.*, Submeter bathymetric mapping of volcanic and hydrothermal features on the East Pacific Rise crest at 9°50′N. *Geochem. Geophys. Geosyst.* **8**, Q01006 (2007).
40. Y. J. Tan, M. Tolstoy, F. Waldhauser, W. S. D. Wilcock, Dynamics of a seafloor-spreading episode at the East Pacific Rise. *Nature* **540**, 261–265 (2016).
41. R. M. Haymon *et al.*, Volcanic eruption of the mid-ocean ridge along the East Pacific Rise crest at 9°45-52′N: Direct submersible observations of seafloor phenomena associated with an eruption event in April, 1991. *Earth Planet. Sci. Lett.* **119**, 85–101 (1993).
42. A. F. Arnulf *et al.*, Anatomy of an active submarine volcano. *Geology* **42**, 655–658 (2014).
43. M. Xu *et al.*, Variations in axial magma lens properties along the East Pacific Rise (930N–1000N) from swath 3-D seismic imaging and 1-D waveform inversion. *J. Geophys. Res. Solid Earth* **119**, 2721–2744 (2014).
44. O. Aghaei *et al.*, Constraints on melt content of off-axis magma lenses at the East Pacific Rise from analysis of 3-D seismic amplitude variation with angle of incidence. *J. Geophys. Res. Solid Earth* **122**, 4123–4142 (2017).
45. R. J. Varga, J. S. Gee, L. Bettison-Varga, R. S. Anderson, C. L. Johnson, Early establishment of seafloor hydrothermal systems during structural extension: Paleomagnetic evidence from the Troodos ophiolite, Cyprus. *Earth Planet. Sci. Lett.* **171**, 221–235 (1999).
46. M. T. Gudmundsson, F. Sigmundsson, H. Björnsson, Ice-volcano interaction of the 1996 Gjalp subglacial eruption, Vatnajokull, Iceland. *Nature* **389**, 954–957 (1997).
47. V. Acocella, D. Trippanera, How diking affects the tectonomagmatic evolution of slow spreading plate boundaries: Overview and model. *Geosphere* **12**, 867–883 (2016).
48. W. Xu, S. Jónsson, F. Corbi, E. Rivalta, Graben formation and dike arrest during the 2009 Harrat Lunayyir dike intrusion in Saudi Arabia: Insights from InSAR, stress calculations and analog experiments. *J. Geophys. Res. Solid Earth* **121**, 2837–2851 (2016).
49. D. D. Pollard, A. Aydin, Propagation and linkage of oceanic ridge segments. *J. Geophys. Res.* **89**, 10017–10028 (1984).
50. J. Mutter *et al.*, Multi-Channel Seismic Shot Data from the East Pacific Rise 9 Degrees North Spreading Center Segment acquired during R/V Marcus G. Langseth expedition MGL0812 (2008). Interdisciplinary Earth Data Alliance (IEDA). 10.1594/IEDA/314654. Deposited 11 February 2010.
51. R. Parnell-Turner *et al.*, Processed bathymetric data (netCDF grid) from 9°50′N, East Pacific Rise, acquired in 2018, 2019 and 2021 during AUV Sentry near-bottom dives. Interdisciplinary *Earth* Data Alliance (IEDA). https://doi.org/10.26022/IEDA/330373. Deposited 14 October 2021.
52. M. Marjanovic, Axial Magma Lens horizon beneath the eruption area of the East Pacific Rise 9°50′N. Interdisciplinary Earth Data Alliance (IEDA). 10.26022/IEDA/331330. Deposited 27 July 2023.
53. M. Marjanovic, Axial Magma Lens horizon from a 3-D seismic volume for the segment south of the East Pacific Rise 9°50′N eruption area. Marine Geoscience Data System (MGDS). 10.60521/331596. Deposited 28 March 2024.